Research Square

Preprints are preliminary reports that have not undergone peer review.
They should not be considered conclusive, used to inform clinical practice,
or referenced by the media as validated information.

Integrated bioinformatic analysis identifies distinct neddylation-associated proteasome genes and immune-related features in laryngeal squamous cell carcinoma

Shujuan Wang
The Affiliated Cancer Hospital of Zhengzhou University, Henan Cancer Hospital
Jing Xu
The Affiliated Cancer Hospital of Zhengzhou University, Henan Cancer Hospital
Hong Ge
gehong616@126.com
The Affiliated Cancer Hospital of Zhengzhou University, Henan Cancer Hospital

Article

Keywords: laryngeal squamous cell carcinoma, neddylation, proteasome, KCTD6, immune infiltration, bile acid metabolism

Posted Date: September 7th, 2026

DOI: https://doi.org/10.21203/rs.3.rs-10736013/v1

License: This work is licensed under a Creative Commons Attribution 4.0 International License.
Read Full License

Additional Declarations: No competing interests reported.

Abstract

Neddylation contributes to cancer progression, but its relationship with proteasome-related genes and the immune microenvironment in laryngeal squamous cell carcinoma (LSCC) remains unclear. We aimed to identify neddylation-associated genes in LSCC and characterize their molecular, metabolic, and immune features. Transcriptomic data from The Cancer Genome Atlas and Gene Expression Omnibus were analyzed using differential expression, functional enrichment, and machine-learning approaches. Key genes were further evaluated by survival, pathway, immune infiltration, and somatic mutation analyses and validated by quantitative real-time PCR (qRT-PCR) in five paired LSCC and adjacent tissues. Seventy-four differentially expressed neddylation-related genes were identified. Four genes, KCTD6, PSMB2, PSMB4, and PSMD2, were selected by both LASSO and SVM-RFE. KCTD6-associated genes were enriched in bile acid metabolism, while macrophage M0 and resting CD4 + memory T cells were associated with prognosis. Lower PSMB4 and PSMD2 expression was associated with immune escape-related features. qRT-PCR showed concordant expression patterns, with KCTD6 downregulated and PSMB2, PSMB4, and PSMD2 upregulated in tumors; only PSMB2 reached statistical significance. We identified a distinct set of proteasome-related neddylation-associated genes associated with metabolic and immune characteristics in LSCC. These findings suggest potential links between neddylation-associated proteasome genes and the immune microenvironment in LSCC.

1. Introduction

Laryngeal squamous cell carcinoma (LSCC) accounts for 85–95% of laryngeal cancers, with over 184,000 new cases diagnosed worldwide each year. Histologically, LSCC shows infiltrative growth of dyskeratotic squamous epithelium and is often accompanied by early cervical lymph-node metastasis (1). Mortality rates range from 40% to 50%, and among individuals with smoking-related and human papillomavirus (HPV)-negative disease, the 5-year survival rate falls below 40% (2, 3). Although surgery combined with chemoradiotherapy can achieve five-year survival rates of 70–90% in early-stage disease, patients with advanced LSCC have survival rates below 35% and laryngeal preservation rates as low as 20%, often causing severe respiratory and swallowing dysfunction (4). These clinical challenges underscore the need to better define molecular mechanisms driving LSCC progression and identify targets that may improve risk stratification and clinical decision-making.

Neddylation is a reversible post-translational modification in which NEDD8 is covalently conjugated to substrate proteins, primarily cullin family members, thereby regulating the activity of cullin-RING E3 ubiquitin ligases (CRLs). By modulating protein ubiquitination and degradation, neddylation is required for maintaining cellular homeostasis, including cell-cycle regulation, DNA damage response, and signal transduction (5, 6). In malignant tumors, aberrant hyper-neddylation stabilizes oncoproteins such as c-Myc and EGFR and sustains oncogenic signaling pathways, including PI3K/AKT, thereby promoting immune evasion and chemoresistance (6, 7). In head and neck squamous cell carcinoma, NAE1 and NEDD8 are significantly upregulated and positively associated with TNM stage (8). However, LSCC-

specific neddylation-related gene patterns and their relationship with the tumor microenvironment remain incompletely defined (9).

A recent bioinformatic study has examined neddylation-related genes (NRGs) in LSCC, but with different gene sets and endpoints. Wang et al. (10) developed a neddylation-associated prognostic signature based on COMMD2, WSB2, and CUL9 and further examined ribosome-related pathways, immune infiltration patterns, and regulatory microRNA networks, with experimental validation of selected targets. Although that work provided important insight into the prognostic significance of neddylation in LSCC, the analyzed gene set and biological emphasis differ from those of the present study. Specifically, Wang et al. focused on cullin-related neddylation genes and ribosome pathways, whereas the present analysis emphasizes proteasome-associated neddylation genes and their links to bile acid metabolism and immune cell infiltration.

In contrast, the present study focuses on a distinct subset of neddylation-associated genes closely linked to the proteasome and ubiquitin-proteasome system, including KCTD6 and specific PSMB and PSMD subunits. Given the functional coupling among neddylation, CRL activity, and proteasome-mediated protein turnover, proteasome-related neddylation-associated genes were hypothesized to have distinct biological and immune associations in LSCC. In addition to survival analyses, complementary biological features were examined, including bile acid metabolism-related pathways and immune cell infiltration patterns, particularly macrophage M0 and resting CD4 + memory T cells. Immune escape-related features inferred by computational prediction algorithms were also evaluated.

We performed integrated bioinformatic analyses of LSCC transcriptomic datasets from The Cancer Genome Atlas (TCGA) and the Gene Expression Omnibus (GEO) to identify neddylation-associated candidate genes. By combining differential expression analysis, protein-protein interaction network construction, functional enrichment analysis, and machine-learning-based feature selection, proteasome-related neddylation-associated genes were prioritized and then preliminarily validated by quantitative real-time PCR in LSCC tissues. These findings indicate that proteasome-related neddylation-associated genes may be linked to immune and metabolic features in LSCC and are supported by preliminary quantitative real-time PCR validation in clinical tissue samples.

2. Results

2.1 Identification of neddylation-related differentially expressed genes in LSCC

We first compared tumor and normal tissues in the TCGA-LSCC cohort. A total of 7,255 differentially expressed genes (DEGs) were identified (Figs. 1A and 1B, Supplementary Table S1). Intersecting these DEGs with 245 neddylation-related genes yielded 74 differentially expressed neddylation-related genes (DE-NRGs) (Fig. 1C, Supplementary Table S2). Functional enrichment analysis indicated that these DE-NRGs were enriched mainly in proteasome-mediated ubiquitin-dependent protein catabolic processes

and ubiquitin ligase complexes (Fig. 1D). DE-NRGs were also enriched in ubiquitin-mediated proteolysis and disease-associated gene sets, including spinocerebellar ataxia and Parkinson disease (Fig. 1E).

2.2 Protein-protein interaction network construction and candidate gene screening

A PPI network was built to map functional relationships among DE-NRGs. The network showed extensive interactions among DE-NRG-encoded proteins, including CCDC8-BIRC5 and FBXW11-FBXO2 (Fig. 1F), supporting the involvement of ubiquitin-proteasome system components. Key gene modules identified by MCODE analysis (Fig. 1G) were enriched in proteasome and cullin-RING ligase pathways (Figs. 1H and 1I).

2.3 Machine-learning feature selection

Two independent algorithms, LASSO and SVM-RFE, filtered the 40 MCODE genes. When lambda-min was 0.00474, the LASSO model achieved the lowest residual sum of squares and identified ten feature genes (PSMB2, PSMB4, CUL3, KCTD6, PSMD2, KCTD7, ZBTB16, UBC, KBTBD6, and HIF1A) (Fig. 2A). SVM-RFE peaked at nine features (PSMD2, PSMB4, PSMB3, KCTD6, COMMD2, PSMA6, PSMA7, PSMB2, and UBXN7) (Figs. 2B and 2C). Four genes, KCTD6, PSMB2, PSMB4, and PSMD2, survived both LASSO and SVM-RFE filters and were retained as final candidates (Fig. 2D). Both TCGA-LSCC and GSE142083 datasets showed the same pattern: KCTD6 was lower in tumors while PSMB2, PSMB4, and PSMD2 were higher (Figs. 2E and 2F).

2.4 Nomogram construction and survival analysis

ROC curves were generated for each candidate gene (Figs. 3A-3D). A nomogram was constructed to assess discriminative performance based on candidate gene expression in the TCGA-LSCC cohort (Fig. 3E). The calibration, decision, and ROC curves suggested that the nomogram may help distinguish LSCC from normal samples in the TCGA cohort, with better performance than the individual candidate genes (Figs. 3F-3H). Patients in the TCGA-LSCC cohort were stratified into high- and low-expression groups according to each candidate gene. Survival analysis showed that only PSMB2 expression correlated significantly with overall survival in LSCC (Figs. 4A-4D). Correlation analysis showed that KCTD6 was negatively correlated with PSMB2, PSMB4, and PSMD2 (Fig. 4E). The gene-gene interaction network showed interactions between the candidate genes and multiple proteasome-associated genes, including UBLCP1, PSMC1, and KCTD2 (Fig. 4F).

2.5 Functional enrichment and immune infiltration associated with KCTD6 and proteasome-related genes

Genes co-expressed with KCTD6 were enriched in bile acid metabolism-related pathways. Functional enrichment analysis showed that KCTD6, PSMB4, and PSMD2 were co-enriched in myogenesis-related

pathways; PSMB2 and PSMB4 were co-enriched in MYC_TARGETS_V1 and MYC_TARGETS_V2; and KCTD6 and PSMD2 were co-enriched in KRAS-signaling-downregulated pathways (Figs. 5A-5D). GSVA further showed that the HALLMARK_BILE_ACID_METABOLISM pathway was upregulated in the KCTD6 high-expression group, whereas MYC_TARGETS_V1 and MYC_TARGETS_V2 were upregulated in the PSMB2, PSMB4, and PSMD2 high-expression groups but downregulated in the KCTD6 high-expression group (Fig. 5G).

2.6 Immune cell infiltration and survival associations

Immune infiltration analysis was performed to characterize the immune cell composition of LSCC. LSCC samples had a higher proportion of infiltrating B-cell subsets than normal tissues (Fig. 6A), and six immune cell types differed significantly between tumor and normal samples: macrophage M0, macrophage M2, activated mast cells, resting mast cells, resting myeloid dendritic cells, and resting CD4 + memory T cells (Fig. 6B). Macrophage M0 (Fig. 6C, $p = 0.0009$), activated mast cells (Fig. 6E, $p = 0.009$), resting myeloid dendritic cells (Fig. 6G, $p = 0.003$), and resting CD4 + memory T cells (Fig. 6H, $p = 0.027$) were significantly associated with prognosis (Figs. 6C-6H). Correlation analysis further showed that macrophage M0 was negatively correlated with KCTD6 and positively correlated with PSMD2, whereas resting CD4 + memory T cells were negatively correlated with PSMB4 (Supplementary Figure S5).

2.7 Association between PSMB4 / PSMD2 expression and immune escape-related features

TIDE, dysfunction, and exclusion scores were calculated to estimate immunotherapy response. The TIDE and dysfunction scores were higher in the PSMB4 low-expression group, whereas the dysfunction score was higher in the PSMD2 low-expression group (Figs. 7B and 7D), suggesting that reduced PSMB4 and PSMD2 expression may be associated with immune escape-related features. Immune-related molecules, including TNFRSF18 and HLA-A, were associated with candidate gene expression (Supplementary Figures S1–S4). ESTIMATE analysis further showed that the PSMB2 and PSMB4 low-expression groups had higher stromal scores, whereas the KCTD6 high-expression group had higher immune and ESTIMATE scores (Figs. 7E-7H).

2.8 Somatic mutation, CNV, and regulatory network analysis

Somatic mutations and CNV were analyzed to characterize genomic alterations in the four candidates. PSMD2 had a mutation frequency of up to 24%, with amplification as the predominant alteration type. CTD analysis identified reported associations between environmental chemicals, including bisphenol A, benzo[a]pyrene, copper sulfate, and amitrole, and the candidate genes. The ceRNA network suggested potential regulatory relationships, including PSMD2-hsa-miR-361-3p-MALAT1 and KCTD6-hsa-miR-153-3p-SNHG15 (Supplementary Figure S6).

2.9 qRT-PCR validation of candidate gene expression

The four candidate genes were validated by qRT-PCR on five paired LSCC tumor and adjacent non-tumor specimens, using the redesigned primer set described in Methods (Section 4.9.4 and Supplementary Table S3) (Fig. 8). Matching the TCGA and GEO predictions, KCTD6 mRNA expression was lower in LSCC tumor tissues than in adjacent non-tumor tissues (1.920 ± 0.350 vs. 2.835 ± 0.467; P = 0.058), whereas PSMB2, PSMB4, and PSMD2 showed higher expression in tumor tissues than in adjacent non-tumor tissues (PSMB2: 6.690 ± 0.400 vs. 5.250 ± 0.380, P = 0.011; PSMB4: 8.395 ± 0.300 vs. 7.610 ± 0.500, P = 0.095; PSMD2: 8.510 ± 0.687 vs. 7.195 ± 0.260, P = 0.066), as summarized in Supplementary Table S4. Among the four genes, PSMB2 reached statistical significance (P = 0.011); KCTD6, PSMB4, and PSMD2 showed expression trends consistent with the computational predictions but did not clear nominal significance with the present sample size. The direction of expression change for all four genes was concordant with the TCGA and GEO analyses, supporting the reliability of the bioinformatic findings and providing preliminary experimental evidence that these neddylation-associated proteasome genes are dysregulated in LSCC.

3. Discussion

Advanced LSCC carries a 5-year survival below 35% and a laryngeal preservation rate of only 20%, even with combined surgery and chemoradiation (23, 24). Clinicians need markers that catch LSCC earlier and guide treatment, a gap this study begins to address. Neddylation, a post-translational modification that regulates protein stability and signaling through cullin-RING E3 ubiquitin ligases, regulates protein turnover in multiple cancers (25–27). However, the landscape and biological significance of neddylation-related genes in LSCC remain incompletely defined. We therefore combined TCGA and GEO datasets, applied LASSO and SVM-RFE feature selection, and identified four neddylation-related genes (KCTD6, PSMB2, PSMB4, and PSMD2) whose expression, immune correlations, and prognostic associations we report here.

KCTD6 was downregulated in LSCC tumors in both bioinformatic datasets and in our qPCR cohort. KCTD6 is a substrate adaptor for cullin-3 (CUL3) E3 ubiquitin ligase complexes; loss of KCTD6 stabilizes oncoproteins that would otherwise be tagged for proteasomal degradation, a mechanism well-described for cullin-RING substrate adaptors (28). Whether KCTD6 loss in LSCC similarly promotes oncoprotein accumulation will require functional studies. Mechanistically, the CRL3/KCTD-family adaptor system places KCTD6 within the same neddylation-CRL-proteasome axis as the PSMB and PSMD subunits identified by our screen (29, 30).

The three proteasome genes told the opposite story: all three were higher in tumors. Overexpression of these subunits speeds degradation of cell-cycle brakes such as p21 and p27. He et al. (31) showed this for PSMB2 in glioma, and Lin et al. (32) demonstrated that PSMB4 reduction in T24 and J82 bladder cancer cells inhibits the angiogenesis and migration of endothelial cells. Li et al. (33) showed that PSMD2 regulates breast cancer cell proliferation and cell-cycle progression by modulating proteasomal

degradation of p21 and p27. PSMD2 overexpression also predicts poor outcomes in esophageal squamous cell carcinoma (34) and in breast cancer (33). Functional pathway analyses in the present study showed that these proteasome-related genes were associated with MYC signaling, consistent with the model that excess proteasome activity clears tumor suppressors faster than they can act (35). Higher PSMB2 correlated with better overall survival in the TCGA-LSCC cohort, a paradox suggesting proteasome components have context-dependent, possibly opposing roles in different cancers (31–33).

How immune cells infiltrate LSCC tumors directly affects both prognosis and immunotherapy eligibility. Immune infiltration analysis showed that macrophage M0 and resting CD4 + memory T cells correlated significantly with prognosis, matching their known roles in tumor immune evasion (36–38). These data indicate that immune cell composition may interact with neddylation-related gene expression patterns in LSCC. To further assess immunotherapy-related features, immune dysfunction and exclusion scores were inferred using the TIDE algorithm (39). The results showed that low PSMB4 and PSMD2 expression was associated with higher immune dysfunction scores, suggesting a potential link between proteasome-related gene expression and immune escape-related features. ESTIMATE analysis showed that higher KCTD6 expression correlated with increased immune and ESTIMATE scores, indicating a relatively immune-enriched tumor microenvironment that may be more responsive to immunotherapeutic strategies (40). Because these immune characteristics were inferred computationally, further experimental validation is needed to confirm their biological and clinical significance. Correlation analyses further showed that macrophage M0 infiltration was negatively correlated with KCTD6 expression and positively correlated with PSMD2 expression, whereas resting CD4 + memory T cells were negatively correlated with PSMB4 expression. These associations suggest that neddylation-associated genes may influence immune cell distribution within the LSCC microenvironment, although causality cannot be established from the current analyses.

Mutation rates for PSMB2, PSMB4, and KCTD6 were low. PSMD2, by contrast, showed copy number amplification in 24% of cases, similar to what has been reported in breast cancer (33) and esophageal squamous cell carcinoma (34). Enrichment analysis placed all four genes within ubiquitin-mediated proteolysis and NF-kappaB signaling pathways, both with established oncogenic roles in head and neck SCC. High-PSMD2 tumors had fewer CD8 + T cells and more M2 macrophages, a pattern that typically signals immune suppression and poor checkpoint-inhibitor response (41). Together, these data suggest that proteasome overactivity may help LSCC tumors dodge immune surveillance. Chemical-gene interaction analysis identified associations between candidate genes and environmental chemicals, including bisphenol A (42), benzo[a]pyrene (43), copper sulfate (44), and amitrole (45). These associations should be interpreted as potential environmental exposure-related risk modifiers rather than direct therapeutic agents and provide additional context for understanding neddylation-proteasome pathway dysregulation in LSCC.

To check whether the TCGA patterns hold in real tissue, qRT-PCR was run on five matched tumor / adjacent pairs from Zhengzhou University using primers redesigned against the canonical RefSeq mRNA of each human gene (Supplementary Table S3). KCTD6 mRNA was lower in tumors and PSMB2, PSMB4,

and PSMD2 were higher. PSMB2 reached statistical significance (P = 0.011); the other three showed expression trends in the predicted direction without clearing nominal significance, which is unsurprising with five paired specimens. Four-for-four directional agreement between TCGA predictions and bench data is encouraging, but a powered confirmatory cohort (n > 20) is needed before calling these true biomarkers.

Three caveats apply. First, the qRT-PCR validation used only five paired specimens; while sufficient to confirm direction of change, this is underpowered for robust effect-size estimation, and immunohistochemistry or Western blot on a larger cohort (n > 30) would resolve whether mRNA changes translate to protein. Second, the small number of normal samples in the TCGA dataset may limit the robustness of the differential expression analyses. Third, although associations with prognosis, immune features, and metabolic pathways were identified, functional experiments are needed to clarify the underlying biological mechanisms and clinical relevance.

4. Materials and methods

4.1 Data sources and neddylation-related gene set

Transcriptomic data, clinical features, somatic mutation profiles, copy number variation (CNV) data, and survival data for LSCC were retrieved from the TCGA database (http://cancergenome.nih.gov/), including 111 tumor samples and 12 normal samples. In addition, the independent LSCC dataset GSE142083 (platform GPL20301) was downloaded from the GEO database (https://www.ncbi.nlm.nih.gov/geo/), comprising 53 tumor samples and 53 normal samples. A total of 245 neddylation-related genes (NRGs) were retrieved from the Reactome database (https://reactome.org). NRGs were defined as genes annotated to the neddylation pathway or related biological processes. Although neddylation directly regulates CRL activity, CRL-mediated ubiquitination ultimately converges on proteasome-dependent protein degradation. Accordingly, genes functionally linked to the ubiquitin-proteasome system were retained when identified through the NRG-overlap and feature-selection workflow. Proteasome-related genes, including KCTD6, PSMB2, PSMB4, and PSMD2, were therefore considered neddylation-associated candidates in downstream analyses, reflecting the functional coupling among neddylation, CRL activation, and proteasome-mediated substrate turnover.

4.2 Differential expression analysis and functional enrichment

We compared tumor and normal samples in the TCGA-LSCC cohort using DESeq2 v1.38.0 (11). Genes with |log2 fold change| > 0.5 and adjusted P value (padj) < 0.05 were considered differentially expressed. DESeq2 internal size-factor normalization was applied using the default workflow. Differentially expressed genes (DEGs) were visualized using ggplot2 v3.4.3 (12) and ComplexHeatmap v2.14.0 (13). Genes overlapping between the DEGs and the Reactome-derived NRG list were defined as differentially expressed neddylation-related genes (DE-NRGs). Protein-protein interaction (PPI) networks of DE-NRGs

were built with STRING (https://string-db.org/; medium confidence > 0.4) and visualized in Cytoscape. Key functional modules were identified with the Molecular Complex Detection (MCODE) algorithm, and genes within these modules were defined as candidate genes. Gene Ontology (GO) and KEGG enrichment analyses were run with clusterProfiler v4.6.2 (14). Multiple testing correction was applied using the Benjamini-Hochberg false discovery rate method, with qvalueCutoff < 0.05 considered statistically significant.

4.3 Machine-learning-based feature selection

We applied two independent feature-selection algorithms, LASSO regression and SVM-RFE, to prioritize candidates. LASSO regression was performed using the glmnet package v4.1-4, with the optimal regularization parameter (lambda-min) determined by 10-fold cross-validation using cv.glmnet (15). SVM-RFE was performed using the caret package v6.0-93 with 10-fold cross-validation, and the feature set with the highest classification accuracy was selected (16). Genes identified by both LASSO and SVM-RFE were defined as final candidate genes. These genes were then evaluated for differential expression in both the TCGA-LSCC and GSE142083 datasets. Genes with consistent expression trends and statistically significant differences between tumor and normal tissues in both datasets were retained for downstream analyses.

4.4 Diagnostic value and prognostic association analyses

We generated receiver operating characteristic (ROC) curves with pROC v1.18.0 to assess the diagnostic performance of candidate genes (17). Nomograms were constructed using rms v6.5-0 based on gene expression data from the TCGA-LSCC cohort (18). Calibration curves, decision curve analysis, and ROC curves were used to evaluate nomogram performance. For prognostic analysis, patients were categorized into high- and low-expression groups according to candidate gene expression, and Kaplan-Meier survival analysis was performed between groups ($P < 0.05$). Correlations among candidate genes were assessed using Spearman correlation analysis and visualized with corrplot v0.92 (19).

4.5 Pathway-level functional analyses

To investigate functional pathways associated with candidate genes, differential expression analysis between high- and low-expression groups was performed using DESeq2. Gene set enrichment analysis (GSEA) and gene set variation analysis (GSVA) were then used to characterize relevant biological pathways. Using HALLMARK gene sets from the Molecular Signatures Database (MSigDB), genes were ranked by log2 fold change and subjected to GSEA with clusterProfiler (padj < 0.05). GSVA was performed with the GSVA package v1.46.0 (20).

4.6 Tumor immune microenvironment and immunotherapy-related analyses

We estimated immune cell infiltration with CIBERSORT v1.03 ($P < 0.05$) (21). Immune cell types with differential infiltration were further examined for prognostic relevance by stratifying samples into high- and low-infiltration groups, followed by Kaplan-Meier survival analysis. Associations between candidate

gene expression and prognosis-associated immune cells were assessed using Spearman correlation analysis. These analyses were exploratory and were not adjusted for multiple testing. Correlation plots were generated with ggcorrplot v0.1.4 (19). To infer immune escape-related features, the Tumor Immune Dysfunction and Exclusion (TIDE) algorithm was used to calculate TIDE, dysfunction, and exclusion scores in high- and low-expression groups. In addition, expression of immune checkpoint genes, co-stimulatory molecules, MHC genes, chemokines, and their receptors was compared between groups. Immune, stromal, and ESTIMATE scores were calculated using ESTIMATE v1.0.13 (22).

4.7 Prediction of genetic variants, drugs, and molecular regulation

Somatic mutation and CNV data for candidate genes were obtained from the TCGA-LSCC cohort and analyzed using cBioPortal segmentation analysis and the GISTIC algorithm. To generate hypotheses regarding potential chemical-gene interactions, associations between chemicals and candidate genes were examined using the Comparative Toxicogenomics Database (CTD) (http://ctdbase.org/) to identify reported chemical associations. These findings are descriptive and should be interpreted as hypothesis-generating rather than as direct therapeutic predictions. Potential miRNAs targeting candidate genes were predicted using miRanda (http://mirtoolsgallery.tech/mirtoolsgallery/node/1055) and miRDB (http://mirdb.org), and overlapping miRNAs were retained. Candidate lncRNA interactions were obtained from the starBase database (http://starbase.sysu.edu.cn). Regulatory networks were visualized using Cytoscape.

4.8 Statistical analysis

All analyses were performed in R v4.2.2. Two-group comparisons used the Wilcoxon test for non-normally distributed data. Statistical analyses of qRT-PCR data were performed using Welch t-test (Section 4.9.5), which is robust to unequal variance and is appropriate for small samples (n = 5 per group). $P < 0.05$ was considered statistically significant.

4.9 Quantitative real-time PCR (qRT-PCR) validation

4.9.1 Tissue collection

To validate the expression patterns of the four candidate neddylation-associated genes identified through bioinformatic analysis, qRT-PCR was performed on five paired LSCC tumor and adjacent non-tumor tissue specimens. Fresh tissue samples were collected during surgical resection at The Affiliated Cancer Hospital of Zhengzhou University between July 2025 and November 2025. Tissue specimens were immediately rinsed with pre-cooled phosphate-buffered saline, snap-frozen in liquid nitrogen, and stored at -80 degrees C until RNA extraction.

4.9.2 RNA extraction and DNase treatment

Total RNA was extracted with TRIzol Reagent (Invitrogen, Carlsbad, CA, USA) according to the manufacturer instructions. RNA concentration and purity were assessed by spectrophotometry

(A260/A280 ratio), and RNA integrity was confirmed by agarose gel electrophoresis. All RNA samples were treated with RNase-free DNase I (Tiangen Biotech, Beijing, China) for 30 minutes at 37 degrees C to eliminate genomic DNA contamination, followed by enzyme inactivation according to the manufacturer protocol. DNase treatment was applied to every sample regardless of A260/A280 ratio because the beta-actin reference primers used in this study reside in the 3-prime untranslated region (Section 4.9.4) and therefore cannot discriminate cDNA from genomic DNA on amplicon length alone.

4.9.3 cDNA synthesis

cDNA was synthesized from DNase-treated total RNA using the FastQuant RT Kit (Tiangen Biotech, Beijing, China) according to the manufacturer instructions. For each sample, a parallel reaction was prepared with the reverse transcriptase enzyme omitted (no-RT control) to permit assessment of residual genomic DNA in downstream qRT-PCR (Section 4.9.5).

4.9.4 Primer design and quantitative real-time PCR

Primer pairs for the four candidate target genes (KCTD6, PSMB2, PSMB4, PSMD2) and the reference gene beta-actin (ACTB) were designed against the canonical RefSeq mRNA of each human gene using Primer3 (parameters: primer length 18–23 nt, melting temperature 58–62 degrees C, GC content 40–60%, amplicon size 70–200 bp, maximum poly-X 3, GC clamp 1, maximum 3 G/C bases in the last 5 nucleotides at the 3-prime end). For KCTD6, PSMB2, PSMB4, and PSMD2, primer placement was constrained so that the predicted amplicon spans at least one exon-exon junction, ensuring that only complementary DNA derived from mature mRNA is amplified. For ACTB, primers were placed in the 3-prime untranslated region (3-prime UTR) to avoid cross-reactivity with the highly conserved coding region of other actin family members (ACTG1, ACTG2, ACTC1) and the POTE family. Primer specificity was verified by BLAST against the entire human refseq_rna database; for each pair, the intended target gene was confirmed as the unique top hit at 100% identity for both forward and reverse primer, with no off-target transcript producing a predicted amplicon within the 70–300 bp range. Primer sequences and amplicon properties are provided in Supplementary Table S3.

qRT-PCR was performed using SYBR Green Premix Ex Taq II (Takara Bio, Dalian, China) on an Applied Biosystems QuantStudio real-time PCR system (Thermo Fisher Scientific). Each 20 microliter reaction contained 10 microliter of 2x SYBR Green master mix, 0.4 micromolar of each primer, 1 microliter of cDNA (or no-RT control), and nuclease-free water to volume. Cycling conditions were 95 degrees C for 30 seconds (initial denaturation), followed by 40 cycles of 95 degrees C for 5 seconds (denaturation) and 60 degrees C for 30 seconds (combined annealing and extension, with fluorescence acquisition). A melt-curve analysis was performed at the end of every plate (65 to 95 degrees C in 0.5 degrees C steps, 5 seconds per step). Each biological sample was assayed in technical triplicate, with both a no-template control (water) and a no-RT control included on every plate. Wells with multi-peak or shoulder melt curves, or with no-template / no-RT signals less than five cycles later than the lowest-input sample, were excluded from analysis. Amplification efficiency for each primer pair was determined from a 5-step 5-fold serial dilution of pooled cDNA; only pairs with efficiency between 90% and 110% and R-squared > =

0.98 across the standard curve were retained for downstream quantification. Quantification cycle (Cq) values were determined using the QuantStudio software default automatic baseline and threshold setting. Relative mRNA expression was calculated using the 2^(-Delta Delta Ct) method, normalized to beta-actin.

4.9.5 qRT-PCR statistical analysis

Statistical comparisons of relative mRNA expression between tumor and adjacent non-tumor tissues were performed using the Welch t-test, which does not assume equal variance and is appropriate for small samples (n = 5 per group). P values are reported uncorrected for multiple testing, given the limited sample size and the exploratory validation purpose of this analysis. $P < 0.05$ was considered statistically significant.

4.10 Ethics approval and informed consent

The study was approved by the Institutional Ethics Committee of The Affiliated Cancer Hospital of Zhengzhou University (approval number 2023-KY-0129-002, with a 2025 amendment covering the present collection period). All procedures involving human participants were conducted in accordance with the ethical standards of the institutional research committee and with the Declaration of Helsinki and its later amendments. Written informed consent was obtained from all participants prior to tissue collection and analysis.

5. Conclusion

We screened 245 neddylation-related genes across TCGA-LSCC and GEO datasets, and four (KCTD6, PSMB2, PSMB4, PSMD2) passed both LASSO and SVM-RFE filters while showing associations with survival, immune infiltration, and metabolic pathways. qRT-PCR on five paired specimens showed concordant expression directions that KCTD6 was lower and PSMB2, PSMB4, PSMD2 were higher in tumors, matching the computational predictions, with PSMB2 reaching statistical significance. Together, the bioinformatic and qPCR data point to neddylation-proteasome dysregulation as a feature of LSCC, though the qPCR sample (n = 5) is too small for definitive conclusions. Larger cohorts and functional experiments are needed to validate these candidate genes and clarify their biological and clinical relevance in LSCC.

Abbreviations

ceRNA
competing endogenous RNA
CNV
copy number variation
CRLs
cullin-RING E3 ubiquitin ligases
CTD

Comparative Toxicogenomics Database
DEGs
differentially expressed genes
DE-NRGs
differentially expressed neddylation-related genes
ESTIMATE
Estimation of STromal and Immune cells in MAlignant Tumor tissues using Expression data
GEO
Gene Expression Omnibus
GSEA
gene set enrichment analysis
GSVA
gene set variation analysis
LSCC
laryngeal squamous cell carcinoma
MCODE
Molecular Complex Detection
NRGs
neddylation-related genes
PPI
protein-protein interaction
qRT-PCR
quantitative real-time polymerase chain reaction
SVM-RFE
support vector machine-recursive feature elimination
TCGA
The Cancer Genome Atlas
TIDE
Tumor Immune Dysfunction and Exclusion.

Declarations

Competing interests

The authors declare no competing interests.

Funding

This research received no specific grant from any funding agency in the public, commercial, or not-for-profit sectors.

Author Contribution

S.W. and H.G. conceived and designed the study. S.W. and J.X. contributed to data curation, methodology, and investigation. S.W. performed the formal analysis, software implementation, and data visualization. J.X. performed the experimental validation. H.G. supervised the study and was responsible for project administration. S.W. wrote the original draft of the manuscript. J.X. and H.G. reviewed and edited the manuscript. All authors reviewed and approved the final manuscript.

Acknowledgement

The authors gratefully acknowledge the contributors of The Cancer Genome Atlas (TCGA) and the Gene Expression Omnibus (GEO) databases for providing the publicly available data used in this study. We sincerely thank all patients who participated in this study and the clinical staff at The Affiliated Cancer Hospital of Zhengzhou University for their assistance in tissue collection and experimental support.

Data Availability

The publicly available transcriptomic and clinical data analyzed in this study were obtained from The Cancer Genome Atlas (TCGA) and the Gene Expression Omnibus (GEO), including the GSE142083 dataset. Neddylation-related gene sets were obtained from the Reactome database. Data generated from the qRT-PCR experiments and other data supporting the findings of this study are available from the corresponding author upon reasonable request. All relevant processed data are included in the article and its Supplementary Information.

References

1. Liberale, C., Soloperto, D., Marchioni, A., Monzani, D. & Sacchetto, L. Updates on Larynx Cancer: Risk Factors and Oncogenesis. *Int. J. Mol. Sci.* **24** (16), 12913. 10.3390/ijms241612913 (2023).
2. Vander Poorten, V. et al. Salvage surgery for residual or recurrent laryngeal squamous cell carcinoma after (chemo)radiotherapy: oncological outcomes and prognostic factors. *Eur. J. Surg. Oncol.* **47** (11), 2711–2721. 10.1016/j.ejso.2021.05.035 (2021).
3. Zidar, N. et al. The impact of histopathology on prognosis of squamous cell carcinoma of the larynx: can we do better? *Virchows Arch.* **487** (1), 13–32. 10.1007/s00428-025-04082-w (2025).
4. Yanes, M. et al. Laryngeal and pharyngeal squamous cell carcinoma after antireflux surgery in the 5 Nordic countries. *Ann. Surg.* **276** (2), e79–e85. 10.1097/SLA.0000000000004423 (2022).

5. Jiang, Y. et al. Neddylation regulates macrophages and implications for cancer therapy. *Front. Cell. Dev. Biol.* **9**, 681186. 10.3389/fcell.2021.681186 (2021).
6. Zhang, S. et al. Protein neddylation and its role in health and diseases. *Signal. Transduct. Target. Ther.* **9**, 85. 10.1038/s41392-024-01800-9 (2024).
7. Pellegrino, N. E. et al. The next frontier: translational development of ubiquitination, SUMOylation, and NEDDylation in cancer. *Int. J. Mol. Sci.* **23** (7), 3480. 10.3390/ijms23073480 (2022).
8. Paccez, J. D., Foret, C. L. M., de Vasconcellos, J. F., Donaldson, L. & Zerbini, L. F. DCUN1D1 and neddylation: potential targets for cancer therapy. *Biochim. Biophys. Acta Mol. Basis Dis.* **1870** (7), 167308. 10.1016/j.bbadis.2024.167308 (2024).
9. Mao, H., Lin, X. & Sun, Y. Neddylation regulation of immune responses. Research (Wash D C). ;**6**:0283. (2023). 10.34133/research.0283
10. Wang, X., Zhang, H. & Wang, J. Screening and regulatory mechanisms of biomarkers related to neddylation in laryngeal squamous cell carcinoma. *Front. Mol. Biosci.* **12**, 1654064. 10.3389/fmolb.2025.1654064 (2025).
11. Love, M. I., Huber, W. & Anders, S. Moderated estimation of fold change and dispersion for RNA-seq data with DESeq2. *Genome Biol.* **15** (12), 550. 10.1186/s13059-014-0550-8 (2014).
12. Wickham, H. ggplot2: Elegant Graphics for Data Analysis. New York, NY: Springer-Verlag; ISBN: 978-3-319-24277-4. (2016).
13. Gu, Z., Eils, R. & Schlesner, M. Complex heatmaps reveal patterns and correlations in multidimensional genomic data. *Bioinformatics* **32** (18), 2847–2849. 10.1093/bioinformatics/btw313 (2016).
14. Yu, G., Wang, L. G., Han, Y. & He, Q. Y. clusterProfiler: an R package for comparing biological themes among gene clusters. *OMICS* **16** (5), 284–287. 10.1089/omi.2011.0118 (2012).
15. Friedman, J., Hastie, T. & Tibshirani, R. Regularization paths for generalized linear models via coordinate descent. *J. Stat. Softw.* **33** (1), 1–22. 10.18637/jss.v033.i01 (2010).
16. Kuhn, M. Building predictive models in R using the caret package. *J. Stat. Softw.* **28** (5), 1–26. 10.18637/jss.v028.i05 (2008).
17. Robin, X. et al. pROC: an open-source package for R and S + to analyze and compare ROC curves. *BMC Bioinform.* **12**, 77. 10.1186/1471-2105-12-77 (2011).
18. Harrell, F. E. Jr *Regression Modeling Strategies: With Applications to Linear Models, Logistic and Ordinal Regression, and Survival Analysis* 2nd edn (Springer International Publishing, 2015). 10.1007/978-3-319-19425-7
19. Wei, T. & Simko, V. R package corrplot: Visualization of a Correlation Matrix. R package version 0.92. (2021). Available from: https://github.com/taiyun/corrplot
20. Hänzelmann, S., Castelo, R. & Guinney, J. GSVA: gene set variation analysis for microarray and RNA-seq data. *BMC Bioinform.* ;**14**:7. doi:10.1186/1471-2105-14-7. (2013).

21. Newman, A. M. et al. Robust enumeration of cell subsets from tissue expression profiles. *Nat. Methods*. **12** (5), 453–457. 10.1038/nmeth.3337 (2015).
22. Yoshihara, K. et al. Inferring tumour purity and stromal and immune cell admixture from expression data. *Nat. Commun.* **4**, 2612. 10.1038/ncomms3612 (2013).
23. Johnson, D. E. et al. Head and neck squamous cell carcinoma. *Nat. Rev. Dis. Primers*. **6** (1), 92. 10.1038/s41572-020-00224-3 (2020).
24. Sung, H. et al. Global Cancer Statistics 2020: GLOBOCAN estimates of incidence and mortality worldwide for 36 cancers in 185 countries. *CA Cancer J. Clin.* **71** (3), 209–249. 10.3322/caac.21660 (2021).
25. Shao, Y. et al. ALKBH5/YTHDF2-mediated m6A modification of circAFF2 enhances radiosensitivity of colorectal cancer by inhibiting Cullin neddylation. *Clin. Transl Med.* **13** (7), e1318. 10.1002/ctm2.1318 (2023).
26. Wang, T. et al. Advancements in colorectal cancer research: unveiling the cellular and molecular mechanisms of neddylation (Review). *Int. J. Oncol.* **64** (4), 39. 10.3892/ijo.2024.5627 (2024).
27. Zheng, B. et al. Neddylation activated TRIM25 desensitizes triple-negative breast cancer to paclitaxel via TFEB-mediated autophagy. *J. Exp. Clin. Cancer Res.* **43** (1), 177. 10.1186/s13046-024-03085-w (2024).
28. Petroski, M. D. & Deshaies, R. J. Function and regulation of cullin-RING ubiquitin ligases. *Nat. Rev. Mol. Cell. Biol.* **6** (1), 9–20. 10.1038/nrm1547 (2005).
29. Skoblov, M. et al. Protein partners of KCTD proteins provide insights about their functional roles in cell differentiation and vertebrate development. *Bioessays* **35** (7), 586–596. 10.1002/bies.201300002 (2013).
30. Angrisani, A., Di Fiore, A., De Smaele, E. & Moretti, M. The emerging role of the KCTD proteins in cancer. *Cell. Commun. Signal.* **19** (1), 56. 10.1186/s12964-021-00737-8 (2021).
31. He, W. et al. PSMB2 plays an oncogenic role in glioma and correlates to the immune microenvironment. *Sci. Rep.* **14** (1), 5861. 10.1038/s41598-024-56493-5 (2024).
32. Lin, Y. H. et al. The reduction of PSMB4 in T24 and J82 bladder cancer cells inhibits the angiogenesis and migration of endothelial cells. *Int. J. Mol. Sci.* **25** (10), 5559. 10.3390/ijms25105559 (2024).
33. Li, Y. et al. PSMD2 regulates breast cancer cell proliferation and cell cycle progression by modulating p21 and p27 proteasomal degradation. *Cancer Lett.* **430**, 109–122. 10.1016/j.canlet.2018.05.018 (2018).
34. Liu, Y. et al. PSMD2 contributes to the progression of esophageal squamous cell carcinoma by repressing autophagy. *Cell. Biosci.* **13** (1), 67. 10.1186/s13578-023-01016-4 (2023).
35. Ying, K. et al. Diverse Ras-related GTPase DIRAS2, downregulated by PSMD2 in a proteasome-mediated way, inhibits colorectal cancer proliferation by blocking NF-κB signaling. *Int. J. Biol. Sci.* **18** (3), 1039–1050. 10.7150/ijbs.68312 (2022).

36. Huang, C. et al. Identification of novel prognostic markers associated with laryngeal squamous cell carcinoma using comprehensive analysis. *Front. Oncol.* **11**, 779153. 10.3389/fonc.2021.779153 (2022).
37. Yan, L. et al. Identification and validation of immune infiltration phenotypes in laryngeal squamous cell carcinoma by integrative multi-omics analysis. *Front. Immunol.* **13**, 843467. 10.3389/fimmu.2022.843467 (2022).
38. Li, Y., Cai, Q., Shen, X., Chen, X. & Guan, Z. Overexpression of B7-H3 is associated with poor prognosis in laryngeal cancer. *Front. Oncol.* **11**, 759528. 10.3389/fonc.2021.759528 (2021).
39. Wang, X. et al. Construction and validation of immune-related lncRNAs classifier to predict prognosis and immunotherapy response in laryngeal squamous cell carcinoma. *World J. Surg. Oncol.* **20** (1), 164. 10.1186/s12957-022-02608-z (2022).
40. Zhang, M. et al. Construction of a novel disulfidptosis-related lncRNAs signature for prognosis prediction and anti-tumor immunity in laryngeal squamous cell carcinoma. *Heliyon* **10** (10), e30877. 10.1016/j.heliyon.2024.e30877 (2024).
41. Pan, X. et al. Development and validation of a novel endoplasmic reticulum stress-related lncRNA signature in laryngeal squamous cell carcinoma. *Sci. Rep.* **15** (1), 12497. 10.1038/s41598-025-96576-5 (2025).
42. Li, S., Wang, B., Tang, Q., Liu, J. & Yang, X. Bisphenol A triggers proliferation and migration of laryngeal squamous cell carcinoma via GPER-mediated upregulation of IL-6. *Cell. Biochem. Funct.* **35** (4), 209–216. 10.1002/cbf.3265 (2017).
43. Xu, L. et al. Functional polymorphisms in Benzo(a)Pyrene-induced toxicity pathways associated with the risk on laryngeal squamous cell carcinoma. *Food Chem. Toxicol.* **182**, 114199. 10.1016/j.fct.2023.114199 (2023).
44. Wang, M. et al. Anti-cancer potency of copper-doped carbon quantum dots against breast cancer progression. *Int. J. Nanomed.* **19**, 1985–2004. 10.2147/IJN.S449887 (2024).
45. Hurley, P. M. Mode of carcinogenic action of pesticides inducing thyroid follicular cell tumors in rodents. *Environ. Health Perspect.* **106** (8), 437–445. 10.1289/ehp.98106437 (1998).
46. Kanehisa, M. & Goto, S. KEGG: Kyoto Encyclopedia of Genes and Genomes. *Nucleic Acids Res.* **28** (1), 27–30. 10.1093/nar/28.1.27 (2000).

Figures

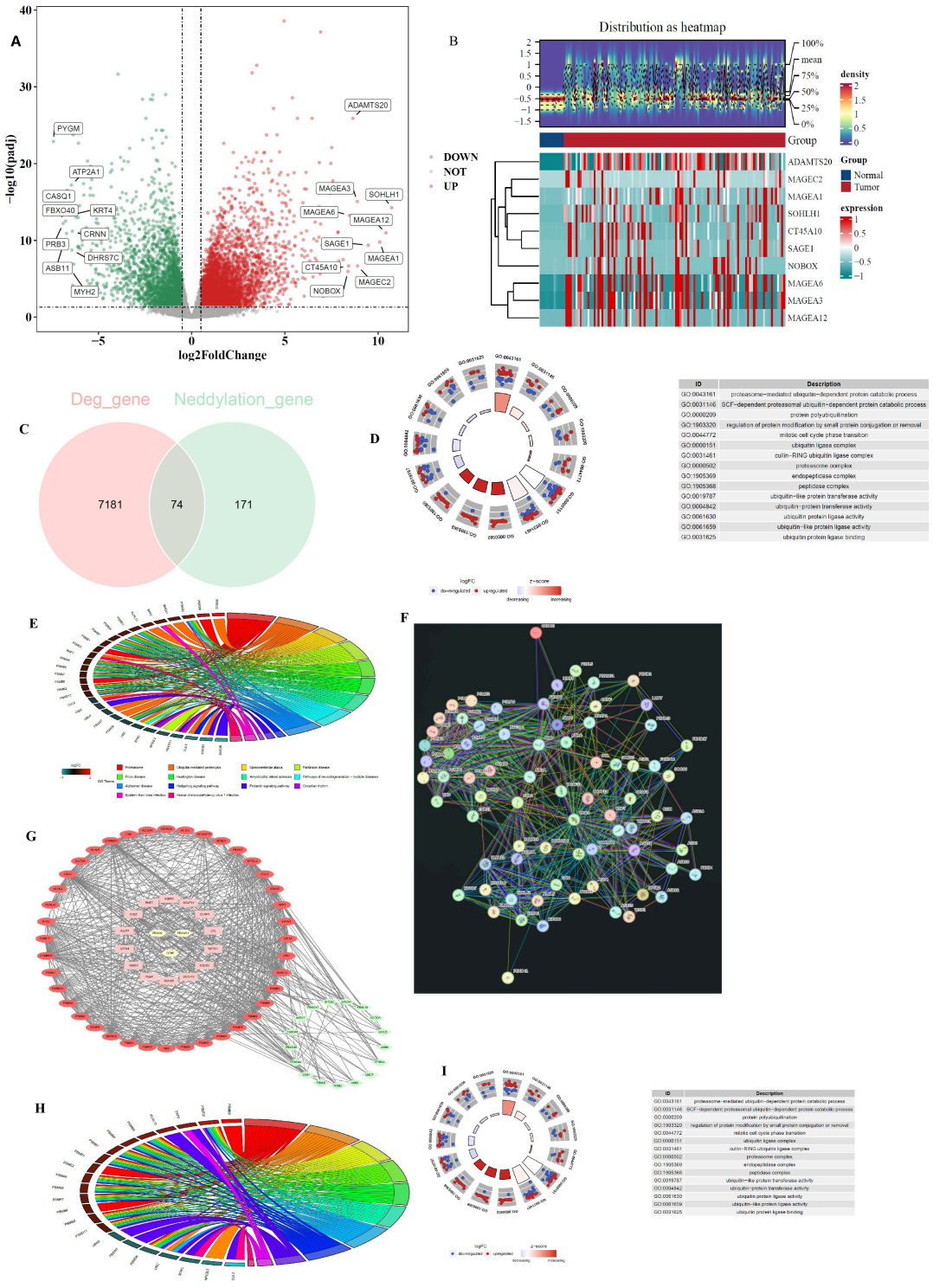


Figure 1

Integrated identification and functional characterization of differentially expressed neddylation-related genes in laryngeal squamous cell carcinoma.

(A) Volcano plot of DEGs between LSCC tumor and normal laryngeal tissues in the TCGA cohort (thresholds: |log2FC| > 0.5, adjusted p < 0.05). Red dots = significantly upregulated genes; green dots =

significantly downregulated genes; representative top-ranked genes are labeled. (B) Heatmap of representative DEGs across LSCC tumor (red) and normal (blue) samples. Rows represent genes grouped by expression direction (upregulated, not significant, downregulated); columns represent individual samples ordered by unsupervised hierarchical clustering. Color intensity reflects scaled expression (red = high, blue = low). (C) Venn diagram showing the overlap between DEGs and neddylation-related genes. Seventy-four genes shared between both sets were taken forward as DE-NRGs for downstream analysis. (D) GO enrichment analysis of the 74 DE-NRGs. Bar length and color represent gene count and GO category, respectively. (E) KEGG pathway enrichment analysis of DE-NRGs, showing enrichment in ubiquitin-mediated proteolysis and disease-associated pathways including spinocerebellar ataxia and Parkinson disease. (F) PPI network of DE-NRGs constructed using STRING. Nodes = proteins; edges = confidence-weighted interactions; key interactions include CCDC8-BIRC5 and FBXW11-FBXO2. (G) Key MCODE-identified gene modules from the PPI network. Color distinguishes individual modules. (H) GO enrichment analysis of genes in key PPI modules, enriched in proteasome and ubiquitin pathways. (I) KEGG pathway enrichment analysis of genes in key PPI modules, enriched in proteasome and cullin-RING ligase pathways. KEGG pathway maps (panels E and I) are reproduced with permission from Kanehisa Laboratories, the copyright holder of the Kyoto Encyclopedia of Genes and Genomes (46).

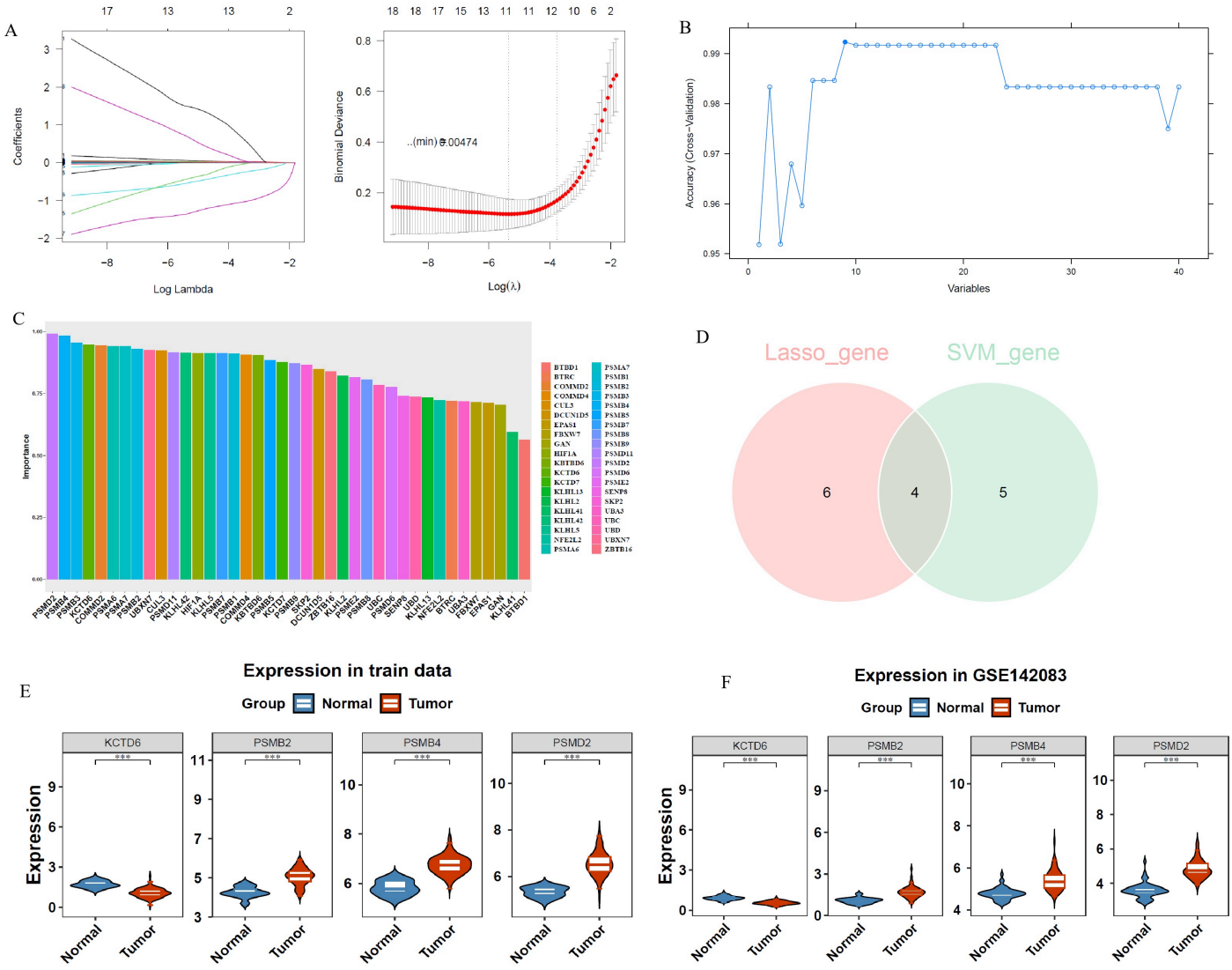


Figure 2

Machine learning-based identification and validation of candidate neddylation-associated genes in laryngeal squamous cell carcinoma.

(A) LASSO regression for feature selection among neddylation-associated genes. Left: regularization paths showing gene coefficient shrinkage as log(lambda) increases. Right: binomial deviance across 10-fold cross-validation; dashed line marks the optimal lambda (lambda.min = 0.00474) at which ten feature genes were retained (PSMB2, PSMB4, CUL3, KCTD6, PSMD2, KCTD7, ZBTB16, UBC, KBTBD6, HIF1A). (B) SVM-RFE cross-validation accuracy curve. Y-axis: 10-fold cross-validation accuracy; x-axis: number of variables retained. Accuracy plateaus (~0.99) when nine variables are included (PSMD2, PSMB4, PSMB3, KCTD6, COMMD2, PSMA6, PSMA7, PSMB2, UBXN7). (C) Relative importance ranking of all neddylation-associated candidate genes derived from the machine learning models. Bar height = relative importance score. (D) Venn diagram showing the overlap between LASSO (n=10) and SVM-RFE (n=9) candidates. Four genes identified by both methods — KCTD6, PSMB2, PSMB4, and PSMD2 — were selected as the final candidate panel (6 LASSO-only, 4 shared, 5 SVM-only). (E) Violin plots of KCTD6, PSMB2, PSMB4,

and PSMD2 expression in normal and tumor samples in the TCGA-LSCC training cohort. All four genes were significantly dysregulated in tumor versus normal tissue (*** p < 0.001). (F) External validation of the four candidate genes in the GSE142083 dataset, confirming consistent expression differences between tumor and normal laryngeal tissue (*** p < 0.001).

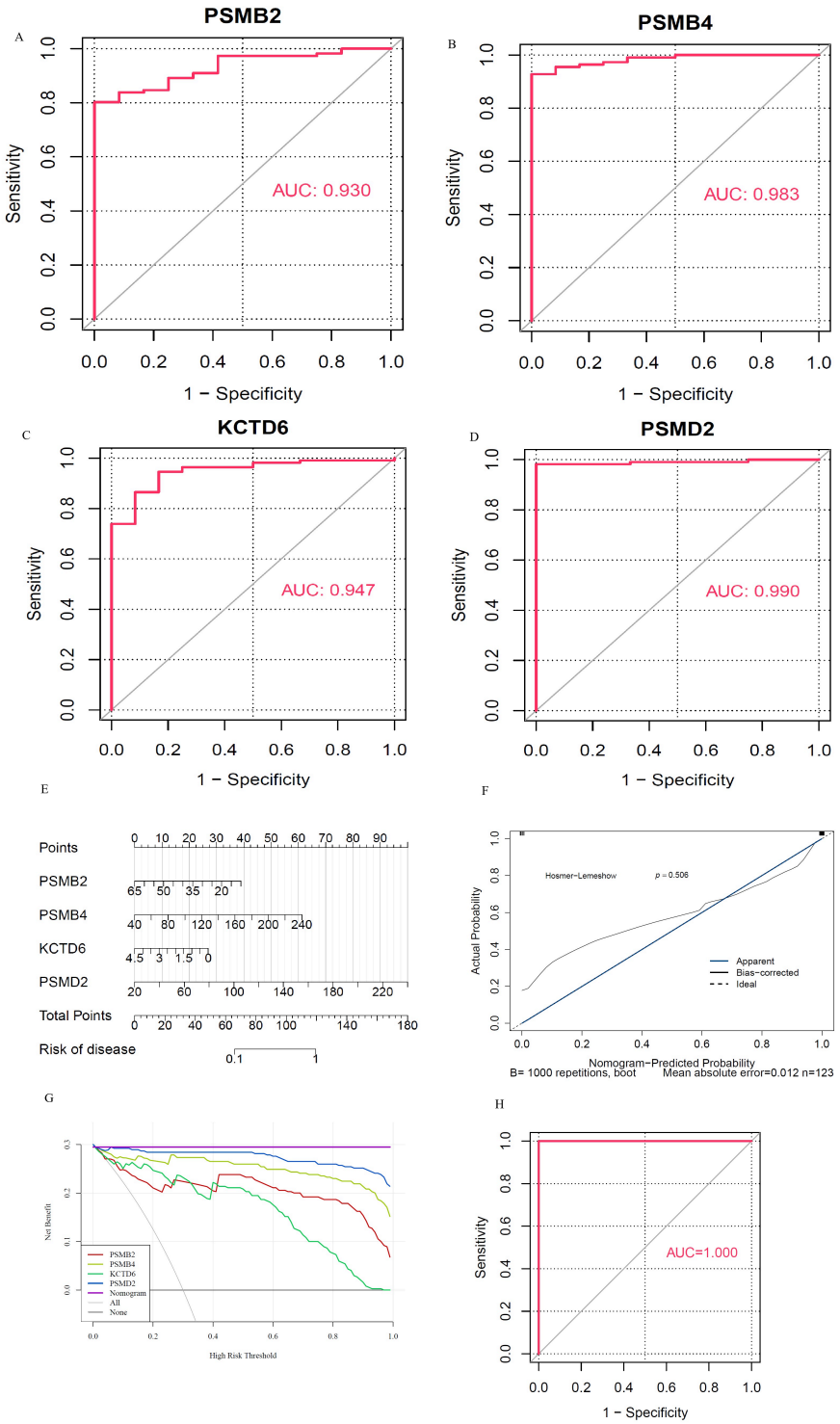


Figure 3

Diagnostic performance and clinical utility assessment of candidate neddylation-associated genes in laryngeal squamous cell carcinoma.

(A) ROC curve for PSMB2 expression distinguishing LSCC from normal samples in the TCGA cohort (AUC = 0.930). (B) ROC curve for PSMB4 expression in the TCGA cohort (AUC = 0.983). (C) ROC curve for KCTD6 expression in the TCGA cohort (AUC = 0.947). (D) ROC curve for PSMD2 expression in the TCGA cohort (AUC = 0.990), the strongest individual discriminator. (E) Nomogram integrating PSMB2, PSMB4, KCTD6, and PSMD2 expression to estimate individual LSCC risk. For each gene, the expression value is projected to the Points axis; all four point values are summed to a Total Points score mapped to the estimated LSCC probability on the Risk of disease scale. (F) Calibration curve comparing nomogram-predicted LSCC probability against observed frequency (1000 bootstrap repetitions, n=123 samples, mean absolute error = 0.012). Close agreement between the bias-corrected and ideal curves indicates good calibration. (G) Decision curve analysis (DCA) assessing the clinical net benefit of the four-gene nomogram across threshold probabilities. The nomogram provides net benefit superior to both Treat All and Treat None reference strategies across the clinically relevant threshold range. (H) ROC curve for the combined four-gene nomogram in the TCGA cohort (AUC = 1.000 in the training cohort; independent validation is required to assess model generalizability.).

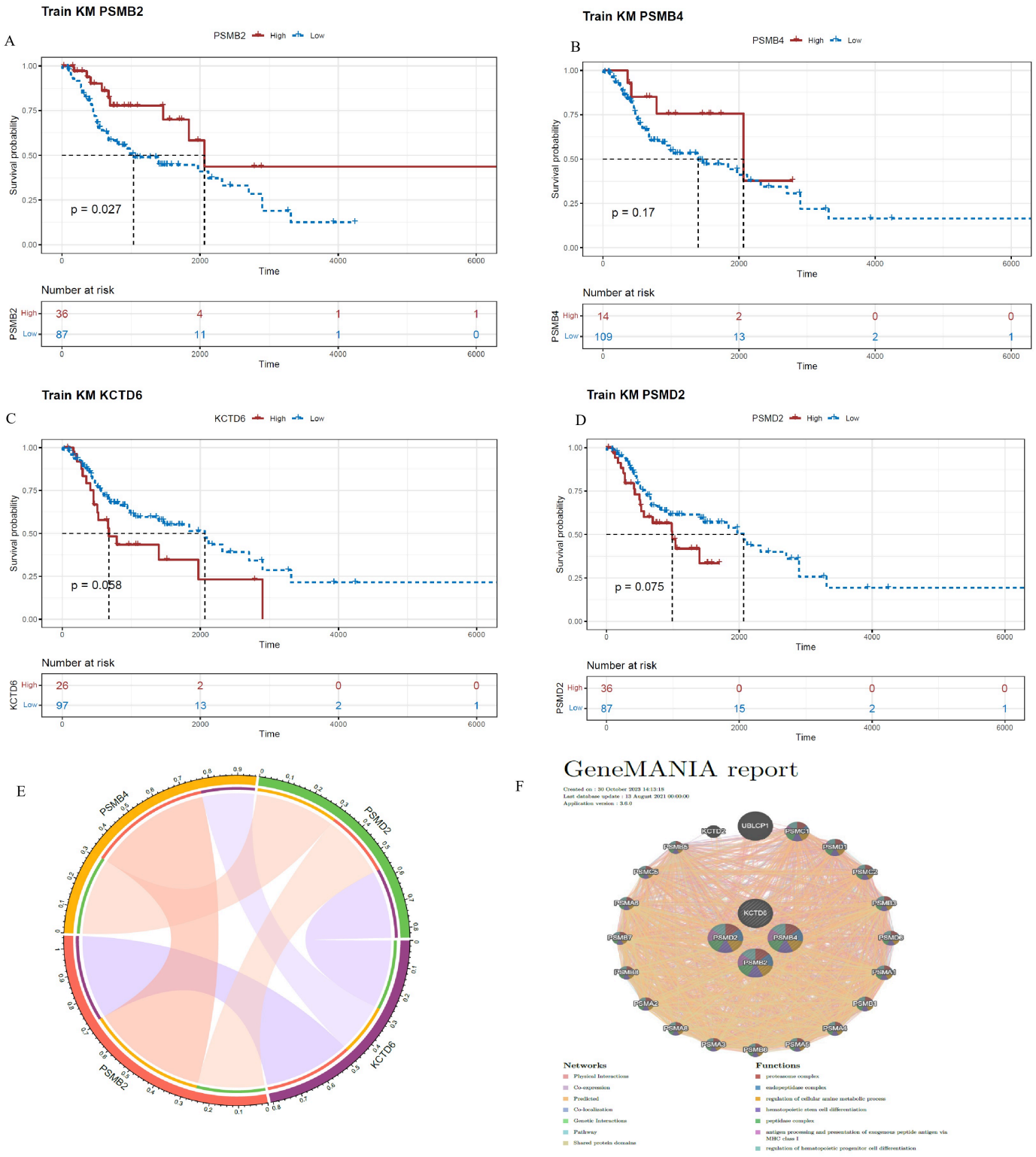


Figure 4

Survival associations and functional network analysis of candidate neddylation-associated genes in laryngeal squamous cell carcinoma.

(A) Kaplan-Meier overall survival analysis comparing high (n=36) versus low (n=87) PSMB2 expression groups in the TCGA-LSCC cohort (log-rank p = 0.027). High PSMB2 expression was significantly

associated with longer overall survival. (B) Kaplan-Meier overall survival analysis for PSMB4 expression groups (high n=14, low n=109; log-rank p = 0.17). No significant difference in overall survival was observed. (C) Kaplan-Meier overall survival analysis for KCTD6 expression groups (high n=26, low n=97; log-rank p = 0.058). A borderline, non-significant trend was observed. (D) Kaplan-Meier overall survival analysis for PSMD2 expression groups (high n=36, low n=87; log-rank p = 0.075). No significant survival difference was detected. Only PSMB2 expression correlated significantly with overall survival among the four candidates. (E) Chord diagram showing pairwise correlations among PSMB2, PSMB4, KCTD6, and PSMD2 expression levels. Arc width and color intensity represent correlation strength. KCTD6 was negatively correlated with PSMB2, PSMB4, and PSMD2. (F) GeneMANIA network showing functional associations between the four candidate genes and related proteasome-associated genes (including UBLCP1, PSMC1, KCTD2). Edge colors represent interaction types: physical interactions, co-expression, co-localization, pathway membership, and shared protein domains. Predicted biological functions include proteasome complex formation and antigen processing and presentation via MHC class I.

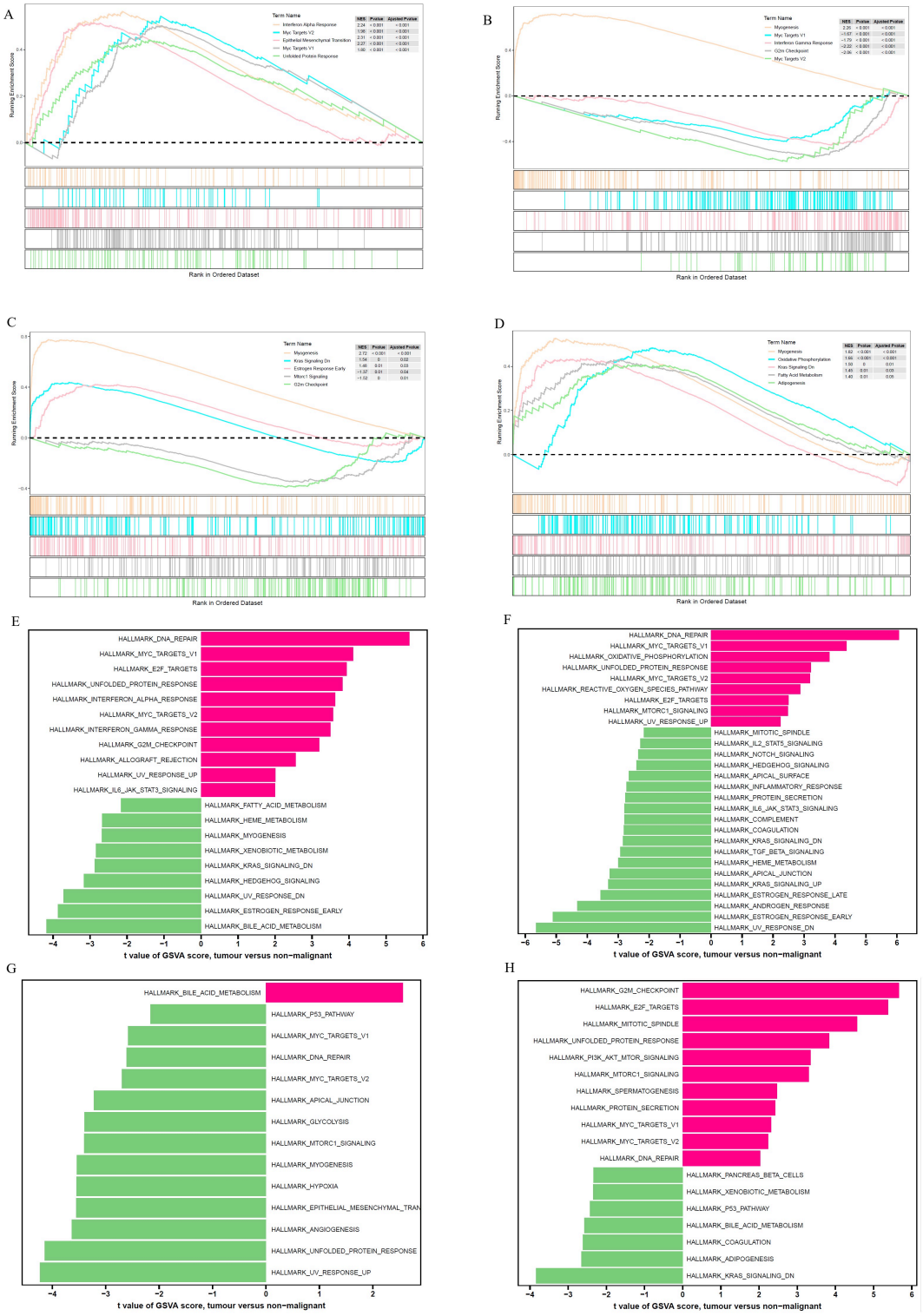


Figure 5

Pathway enrichment patterns associated with candidate neddylation-related genes in laryngeal squamous cell carcinoma.

(A) GSEA of MSigDB hallmark pathways for PSMB2. Each curve = one hallmark gene set enrichment profile. Inset table: NES, nominal p-value, FDR q-value. Significant enrichments include

MYC_TARGETS_V1 and MYC_TARGETS_V2. (B) GSEA for PSMB4: enriched pathways include MYC_TARGETS_V1, MYC_TARGETS_V2, and myogenesis. (C) GSEA for KCTD6: enriched pathways include HALLMARK_BILE_ACID_METABOLISM (upregulated) and KRAS_SIGNALING_DN (co-enriched with PSMD2). (D) GSEA for PSMD2: co-enriched with myogenesis and KRAS_SIGNALING_DN. (E) GSVA showing differential hallmark pathway activity between LSCC tumor and non-malignant laryngeal tissue, stratified by PSMB2 expression. Bars: t-statistic of GSVA scores (tumor vs non-malignant); positive values (magenta) = tumor-enriched; negative values (green) = non-malignant-enriched. MYC_TARGETS_V1 and MYC_TARGETS_V2 upregulated in high-PSMB2 group. (F) GSVA for PSMB4 expression groups: MYC target pathways upregulated in high-PSMB4 tumor tissue. (G) GSVA for KCTD6 expression groups: HALLMARK_BILE_ACID_METABOLISM upregulated; MYC target pathways downregulated in high-KCTD6 group. (H) GSVA for PSMD2 expression groups.

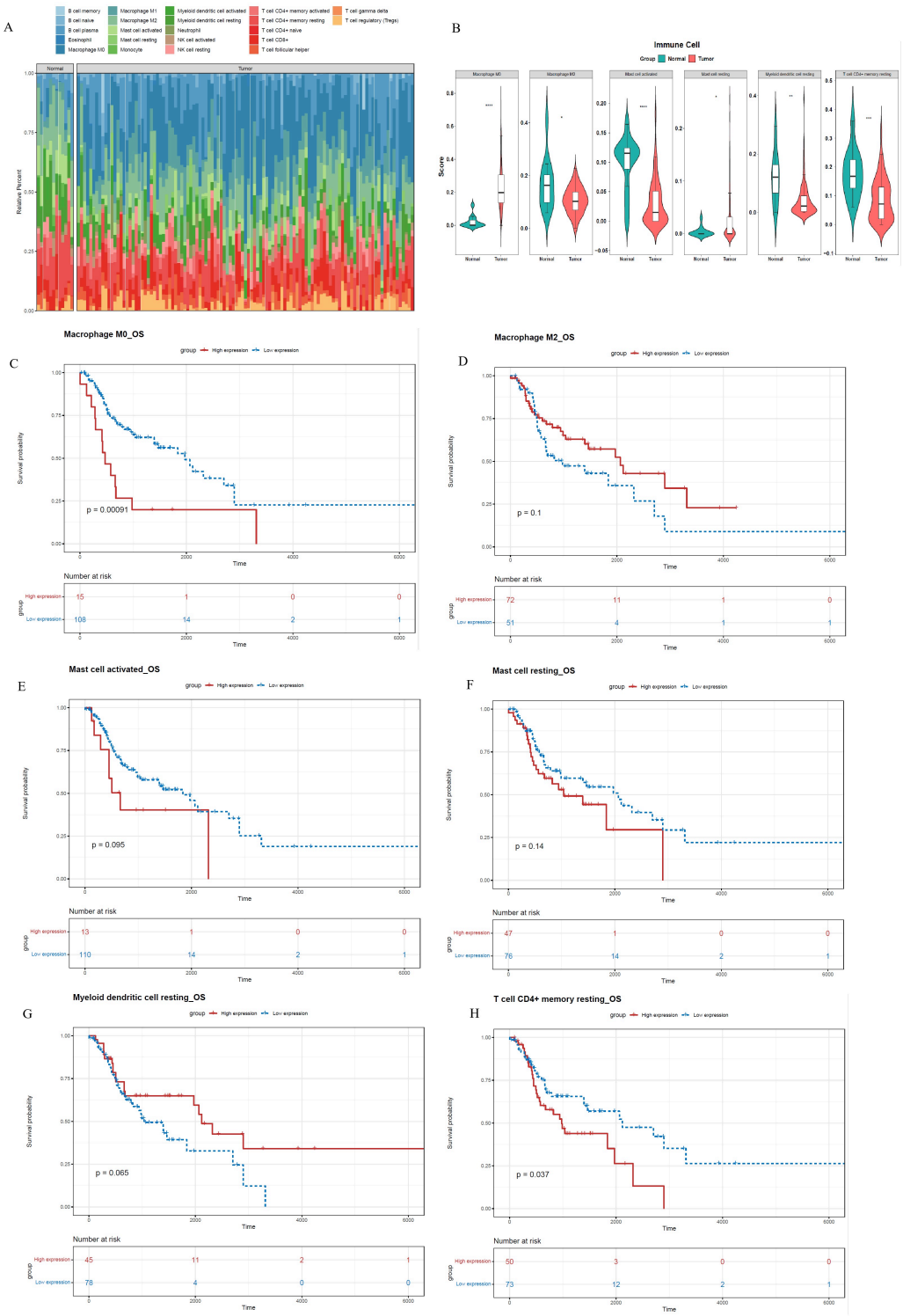


Figure 6

Immune cell infiltration characteristics and survival associations in laryngeal squamous cell carcinoma.

(A) CIBERSORT-based stacked bar chart showing relative immune cell composition (22-cell-type panel) in individual LSCC tumor and normal laryngeal tissue samples. Bar segment height = estimated relative

proportion of each immune cell type. (B) Violin plots comparing estimated abundance of selected immune cell subsets between LSCC and normal laryngeal tissue. Six subsets differed significantly between groups: macrophage M0, macrophage M2, activated mast cells, resting mast cells, resting myeloid dendritic cells, and resting CD4+ memory T cells. (C) Kaplan-Meier overall survival analysis stratified by macrophage M0 infiltration in LSCC (high vs low; log-rank p = 0.0009). High macrophage M0 infiltration was significantly associated with poorer overall survival. (D) Kaplan-Meier overall survival analysis by macrophage M2 infiltration (log-rank p = 0.10); no significant association. (E) Kaplan-Meier overall survival analysis by activated mast-cell infiltration (log-rank p = 0.009); significant association with overall survival. (F) Kaplan-Meier overall survival analysis by resting mast-cell infiltration (log-rank p = 0.114); no significant association. (G) Kaplan-Meier overall survival analysis by resting myeloid dendritic cell infiltration (log-rank p = 0.003); significant association. (H) Kaplan-Meier overall survival analysis by resting CD4+ memory T-cell infiltration (log-rank p = 0.027); significant association.

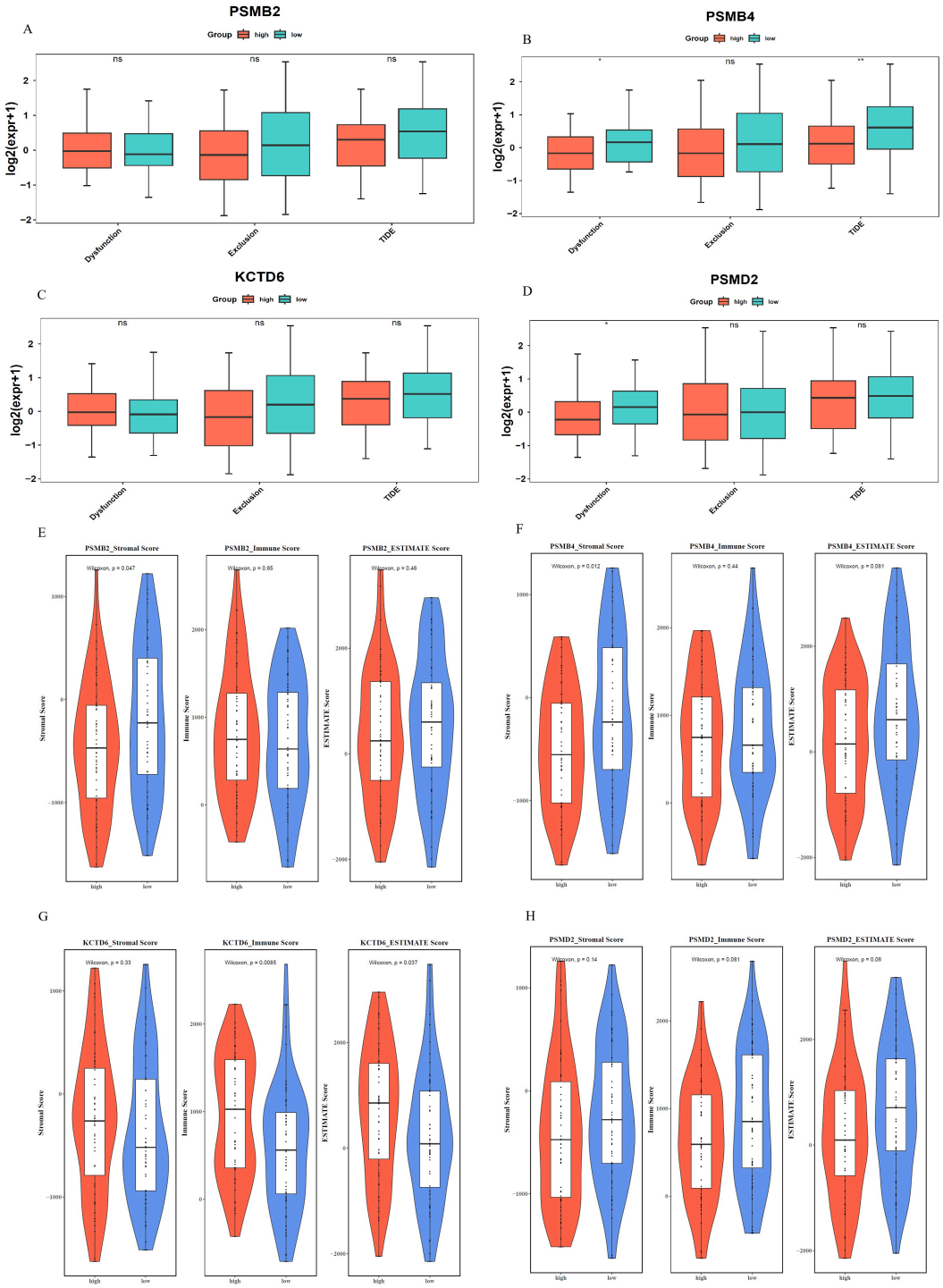


Figure 7

Computational immune dysfunction, immune exclusion, and tumor microenvironment scores associated with candidate neddylation-related gene expression in laryngeal squamous cell carcinoma.

(A) TIDE-based immune dysfunction and exclusion scores stratified by high vs low PSMB2 expression in LSCC. Higher dysfunction scores indicate greater predicted T-cell exhaustion; higher exclusion scores

indicate greater predicted immune exclusion. (B) TIDE-based scores by PSMB4 expression groups. TIDE and dysfunction scores were higher in the low-PSMB4 group, suggesting reduced PSMB4 may be associated with immune escape. (C) TIDE-based scores by KCTD6 expression groups. (D) TIDE-based scores by PSMD2 expression groups. Dysfunction score was higher in the low-PSMD2 group. Statistical significance for all comparisons is indicated by brackets within each panel. (E) ESTIMATE-derived stromal, immune, and ESTIMATE scores compared between high and low PSMB2 expression groups. Low-PSMB2 group had higher stromal scores. (F) ESTIMATE scores by PSMB4 expression groups; low-PSMB4 group had higher stromal scores. (G) ESTIMATE scores by KCTD6 expression groups; high-KCTD6 group had higher immune and ESTIMATE scores. (H) ESTIMATE scores by PSMD2 expression groups.

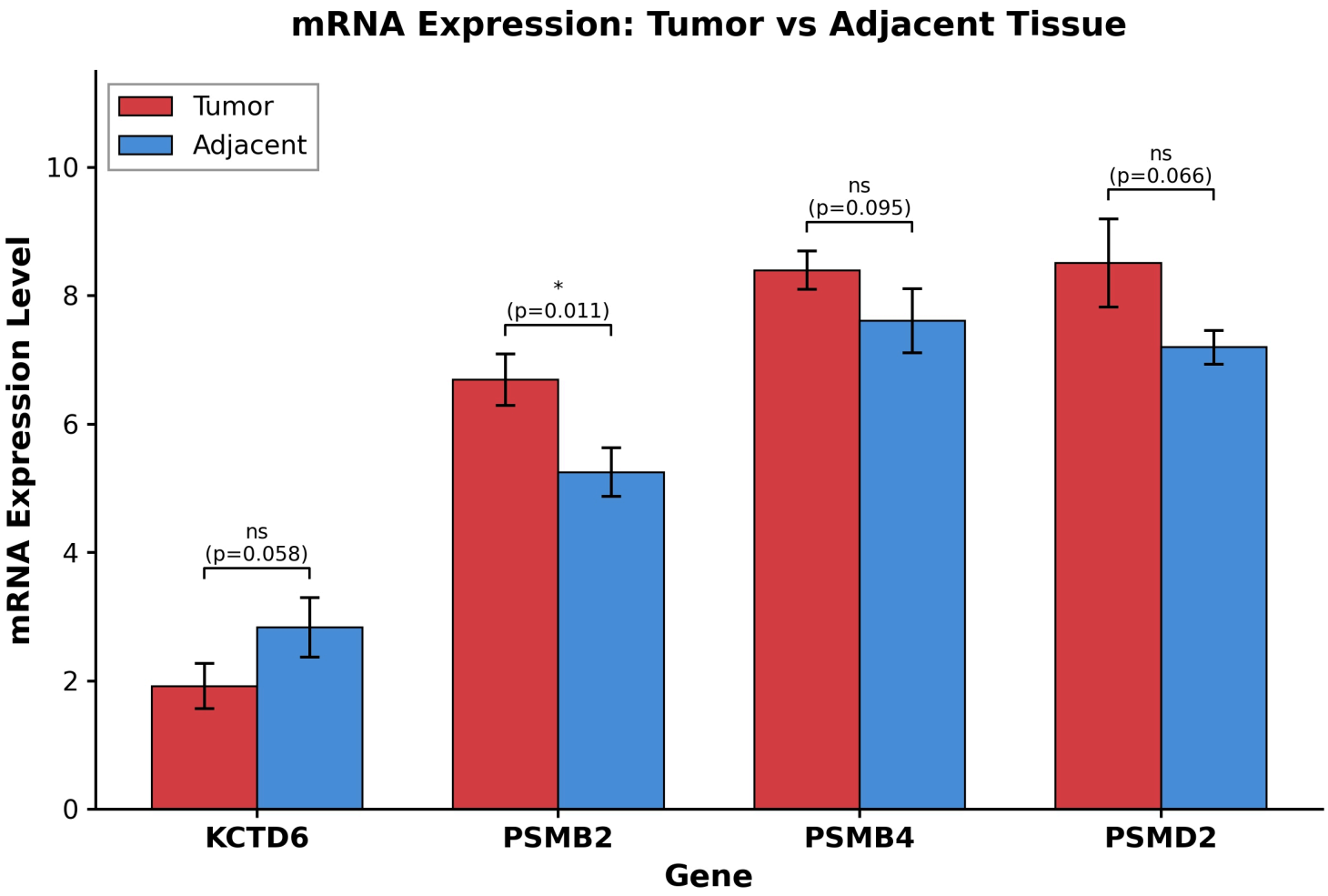


Figure 8

qRT-PCR validation of candidate gene expression in LSCC tissues.

Relative mRNA expression of KCTD6, PSMB2, PSMB4, and PSMD2 was measured in five paired LSCC tumor tissues and adjacent non-tumor tissues by qRT-PCR using the redesigned primer set described in Methods (Section 4.9.4 and Supplementary Table S3). Expression was normalized to β-actin using the 2^(−ΔΔCt) method. Data are presented as mean ± SD across technical triplicate reactions. Statistical

significance was assessed using two-tailed Welch t-test. PSMB2 was significantly upregulated in tumor relative to adjacent tissue ($p = 0.011$). PSMB4 and PSMD2 showed trends toward upregulation that did not reach significance ($p = 0.095$ and $p = 0.066$, respectively). KCTD6 showed a trend toward downregulation in tumor tissue ($p = 0.058$), consistent with the tumor-suppressive direction predicted by computational analyses. The direction of expression change for all four genes was concordant with TCGA and GEO findings. *$P < 0.05$; ns, not significant.

Supplementary Files

This is a list of supplementary files associated with this preprint. Click to download.

- TableS2.xlsx
- TableS1.xlsx
- SupplementaryInformationcorrected.docx